Journal of Solid State Chemistry 324 (2023) 124137

Contents lists available at ScienceDirect

Journal of Solid State Chemistry

journal homepage: www.elsevier.com/locate/jssc

$LaBa_2Fe_3O_8$ cubic perovskite; oxygen-nonstoichiometry defects and conductivity

Pavel Karen

Department of Chemistry, University of Oslo, Blindern, N-0315, Oslo, Norway

ARTICLE INFO

Keywords:
Point defects
Brouwer diagram
Ionic-electronic conductivity
Defect mobility
Transference number
Solid-state diffusion

ABSTRACT

Point defects behind nonstoichiometry of the highly oxygen-vacant $LaBa_2Fe_3^{III}O_8$ single-perovskite structure are studied by quenching a set of nine samples close to Fe^{III} from equilibria at two partial pressures of oxygen, p_{O2}, at four temperatures T. This supports a simplified defect model that fits well the high-temperature electrical conductivity around and below the Fe^{III} point, while deviating somewhat in the oxidized range. The conductivity fitted by sum of its electronic and ionic components versus T and p_{O2} in the surrounding gas reveals a good oxygen-ionic conductor. Oxygen diffusion behind conductivity transients upon a p_{O2} change is discussed.

1. Introduction

While $RBa_2Fe_3^{III}O_8$ of small R = Y [1], Dy [2], Ho [2], and Er [3] are true triple-cell perovskites and have one Fe coordination octahedron per two square pyramids, the R = Gd, Eu, Sm, Nd, and La variants are cubic by powder X-ray diffraction [4,5], while electron microscopy [4,6] reveals some local ordering. Mössbauer spectroscopy of stoichiometric $RBa_2Fe_3^{III}O_8$ [5] shows that upon increasing R, the distribution of Fe polyhedra approaches random (binomial) distribution of three Fe coordinations (square planar, square pyramidal and octahedral), observed [7] in cubic $LaBa_2Fe_3^{III}O_8$ of $^1/_3$ oxygen vacancy per ABO_3 prototype formula. As the ionic size difference of R^{3+} and Ba^{2+} decreases, the nonstoichiometry range widens towards R = La [8].

The wide range and high content of ionic as well as electronic defects per formula are two prerequisites for a high mixed ionic and electronic conductivity that is also favored by the simple cubic structure of $LaBa_2Fe_3^{III}O_8$ with random distribution of all defects. In this study, ionic-defect equilibria of oxygen vacancies are determined *ex situ* via four moderately oxidized and five moderately reduced $LaBa_2Fe_3^{III}O_8$ samples obtained by equilibration in oxidizing and reducing atmospheres at varied temperature followed by quenching. *In situ*, electrical conductivity upon $LaBa_2Fe_3^{III}O_8$ equilibration at isothermal stepwise changes of partial pressure of oxygen at four different temperatures characterizes the energetics behind the mobility and the relative contribution of the electronic and ionic charge carriers. The conductivity transients preceding the equilibria are discussed in terms of the oxygen-exchange kinetics.

2. Experimental

2.1. Synthesis and nonstoichiometry control

The master sample was sintered from precursors obtained by liquid mixing in melted citric acid [9]. The synthesis of the inorganic precursor is described in Ref. [10], except that La_2O_3 (99.9%, Molycorp) is used here. The inorganic-precursor powder was calcined in a corundum boat for 16 h at 1000 °C in flowing O_2. Its pellets were fired two times for 200 h at 1000 °C followed by milling in an agate one-ball vibration mill. Dense cylindrical pellets of about 7 mm in diameter, 10% porosity, and Fe oxidation state 2.97 were obtained by subsequent sintering for 160 h in a flowing gas mixture of volume ratio $Ar/H_2 = 24$, wetted in ~43% H_3PO_4 to obtain the oxygen partial pressure $p_{O2} = 10^{-14.4}$ bar at the sintering temperature 1040 °C. A flat disc for conductivity measurements, cold-pressed from powder at 260 kg/cm^2 to ~40% porosity, sintered during 36 h in flowing O_2 at 1050 °C into 2.3 mm thickness, diameter 20.7 mm, and 30% porosity.

The isothermal equilibration of the cylindrical pellets was performed in a vertical tube furnace at a series of equidistant reciprocal absolute temperatures starting at $0.8 = 1000/T$ (see Table 1 later on) under flowing gas of defined p_{O2} obtained by mixing and wetting described in Ref. [11]. The equilibrium oxygen content of the pellet was quenched by free fall onto a brass flange at the bottom with a counter flow of dried high-purity Ar (<1 ppm O_2). Equilibration in oxidative atmospheres lasted two days, in reductive atmospheres three days.

E-mail address: pavel.karen@kjemi.uio.no.

https://doi.org/10.1016/j.jssc.2023.124137
Received 14 April 2023; Received in revised form 12 May 2023; Accepted 28 May 2023
Available online 29 May 2023

Table 1
Quenching from temperatures t to equilibrate $La_{1/3}Ba_{2/3}FeO_{3-w}$ at two oxygen partial pressures p_{O2}; in gas of volume ratio $R = Ar/O_2$ (top) and Ar/H_2 (bottom), wetted at input to the given p_{H2O}.

$\log_{10}(p_{O2}$/ bar)	t/ °C	R	p_{H2O}/ bar	a/Å	w	Fe ox. state
−3.13	977	1574	0 0165	3.9882 (3)	0.306 (2)	3.055(1)
−3.14	838	1610	0.0170	3.9860 (8)	0.294 (4)	3.078(3)
−3.21	727	1909	0.0170	3.9845 (4)	0.286 (2)	3.094(1)
−3.17	636	1711	0.0165	3.9802 (2)	0.264 (1)	3.138(1)
−15.99	977	13.4	0.0175	3.9942 (1)	0.401 (1)	2.865(2)
−16.01	961	17.7	0.0179	3.9939 (2)	0.391 (1)	2.884(1)
−16.03	946	24.3	0.0174	3.9934 (1)	0.371 (0)	2.924(2)
−16.01	932	33.6	0.0174	3.9932 (1)	0.369 (1)	2.929(0)
−15.98	917	45.4	0.0182	3.9929 (2)	0.367 (1)	2.933(1)

2.2. Characterizations

The oxygen content per formula was determined by cerimetric titration of Fe^{2+} present after digestion of the powdered sample in 5M–6M hydrochloric acid [12], assisted by ultrasound and elevated temperature. Samples oxidized over Fe^{3+} were dissolved (mainly under ultrasound) in presence of ferrous sulfate that was then back titrated. See Ref. [11] for details respecting lab-safety rules. Powder X-ray diffraction was used to check the phase purity and obtain unit-cell parameters from the scanned film from Guinier–Hägg camera with Cu$K\alpha_1$ radiation transmitted through the sample powder with Si internal standard, attached by paraffin oil as a thin layer on a Mylar foil.

2.3. Electrical conductivity measurements

Van der Pauw method [13] was used to measure the electrical conductivity of the flat-disc sample at a constant temperature upon small stepwise changes of the oxygen partial pressure; first upon isothermal reduction (O_2 release) then upon oxidation (O_2 uptake). Each step of the conductivity measurement was a full transient upon diffusion-controlled equilibration of the sample towards its final conductivity at equilibrium with the new composition of the flowing gas. The *in-situ* measurement took place in the hot zone of a vertical tube-furnace, at the same temperatures the oxidized *ex-situ* samples were quenched from. The flat disc of the sample with four equidistant point contacts of gold wire attached around its perimeter was placed at the open end of a wide gas-inlet tube of sintered corundum reaching to the top of an outer closed-end tube of the same material. The gas permeated around the sample in the hot zone to flow back to the outlet at the bottom. In this four-point probe setup, two neighboring contacts pass the measured current while voltage registered on the other two provides the resistance via Ohm's law. The values by the Solartron 1260 frequency-response analyzer measured with 123 Hz alternate current at 1 V potential were corrected for the sample porosity by a factor of the squared ratio of the X-ray density and apparent density taken as weight per outer volume.

3. Results and discussion

3.1. Synthesis

All samples adopted the single-perovskite structure of the $Pm\bar{3}m$ space group, with no trace of impurity lines on the X-ray film. Fig. 1 illustrates the unit cell of the Fe^{III} stoichiometric composition.

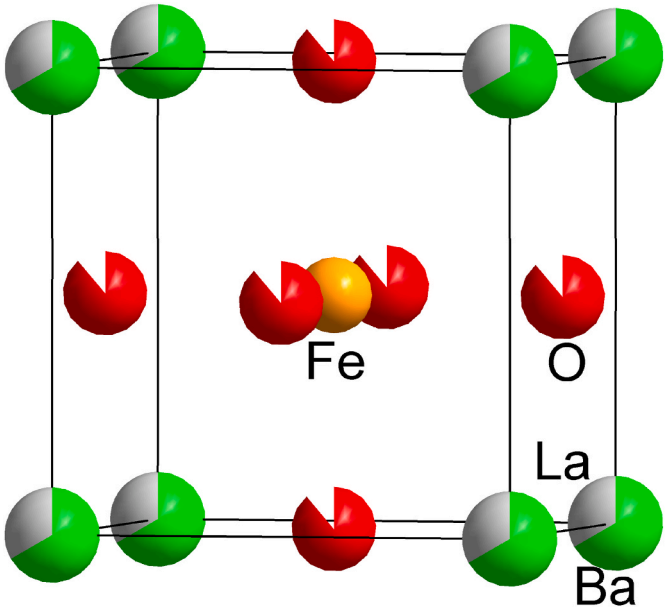

Fig. 1. $La_{1/3}Ba_{2/3}Fe^{III}O_{8/3}$ is a single-perovskite ABO_3 with average A = $^1/_3$La + $^2/_3$Ba and each O ⅑ vacant.

Preliminary tests at high temperatures showed a quick exchange of oxygen between the sample and the surrounding gas. This continues slowly even at room temperature and becomes discernible over a few weeks. Densely sintered pellets were therefore used for quenching. To investigate the variation of the electronic-defect contents around the Fe^{III} point studied *in situ* via conductivity, equilibration was performed in moderately oxidizing and reducing atmospheres ($p_{O2} \approx 10^{-3}$ bar and 10^{-16} bar) at varying temperatures prior quenching to *ex-situ* samples of controlled oxygen-vacancy content. The closeness to Fe^{III} also avoided possible irregularities due to local structural orderings reported in Ref. [6] for heavier-lanthanoid variants of this phase in reducing atmospheres. As the Fe^{III} point corresponds to the $La_{1/3}Ba_{2/3}FeO_{8/3}$ composition in oxygen-vacancy dominated $La_{1/3}Ba_{2/3}FeO_{3-w}$, the latter formula is used in the following.

Oxygen contents of the oxidized quenched samples were calculated from the immediately obtained powder X-ray diffraction data by Vegard rule on a linear fit of a subset of Ref. [8] unit-cell parameters a versus the iron oxidation state. In the set of reduced $La_{1/3}Ba_{2/3}Fe^{III}O_{8/3}$ samples, the a varies less, and cerimetric titration was adopted. Table 1 lists the quenching conditions to obtain the series of samples with a span of moderately oxidized and reduced Fe^{III}.

3.2. The equilibrium of the oxygen exchange

Given the high vacancy content in the samples close to the Fe^{III} stoichiometry, the adopted model of defect equilibria for $La_{1/3}Ba_{2/3}FeO_{3-w}$ concerns randomly distributed ionic defects of oxygen vacancies that participate in the exchange of oxygen with the surrounding atmosphere. In this model, $La_{1/3}Ba_{2/3}FeO_{3-w}$ is taken as a Ba-acceptor doped $LaFeO_3$ perovskite, hence a phase of very low concentration of oxygen interstitials that contribute negligibly to the oxygen content of the *ex situ* samples. Electronic defects (electrons e' and holes $h^\bullet$ in Kröger–Vink notation [14]) have equal concentration in $La_{1/3}Ba_{2/3}Fe^{III}O_{8/3}$. Its oxidation and reduction according to Equations (1) and (2) promotes the appropriate electronic defect upon reaching equilibrium contents per formula (symbolized by square brackets) in the mass-action terms K of the reactions:

$$O_2 + 2V_O^{\bullet\bullet} = 4h^\bullet + 2O_O^\times \quad K_{ox} = [h^\bullet]^4[V_O^{\bullet\bullet}]^{-2}\cdot p_{O2}^{-1} \qquad (1)$$

$$2O_O^{\times} = 4e' + 2V_O^{\bullet\bullet} + O_2 \quad K_{red} = [e']^4[V_O^{\bullet\bullet}]^2 \cdot p_{O2} \tag{2}$$

The holes and electrons are essentially the respective defects $Fe_{Fe}^{\bullet}$ and Fe'_{Fe} and obey the equilibrium intrinsic-ionization reaction:

$$\text{nil} = e' + h^{\bullet} \quad K_i = [e'][h^{\bullet}] \tag{3}$$

The mass-action terms in Equations (1)–(3) correlate as $K_i^4 = K_{ox} \cdot K_{red}$, and electroneutrality condition must be applied:

$$[Ba'_{La}] + [e'] = [h^{\bullet}] + 2[V_O^{\bullet\bullet}] \tag{4}$$

By substituting for $[e']$ and $[h^{\bullet}]$ in Equation (4) from Equations (1) and (2), the $[V_O^{\bullet\bullet}]$ polynomial as a function of the partial pressure of oxygen is expressed:

$$K_{red}^{1/4} + [Ba'_{La}][V_O^{\bullet\bullet}]^{1/2} \cdot p_{O2}^{1/4} - [V_O^{\bullet\bullet}]\, K_{ox}^{1/4} \cdot p_{O2}^{1/2} - 2[V_O^{\bullet\bullet}]^{3/2} \cdot p_{O2}^{1/4} = 0 \tag{5}$$

Reaction enthalpies and entropies then replace the two defect-equilibrium constants in order to include temperature:

$$K_m = \exp(\Delta S_m/R - \Delta H_m/RT); \quad m = \text{ox, red} \tag{6}$$

The experimental $w = [V_O^{\bullet\bullet}]$ in the quenched $La_{1/3}Ba_{2/3}FeO_{3-w}$ samples were fit by least squares against p_{O2} and T in the resulting polynomial that was solved numerically by the bisection method of repeated halving the interval that appears closer to zeroing it. Contents $[e']$ and $[h^{\bullet}]$ per formula were plotted from the fitted parameters and Equations (1), (2) and (6). The refined parameters are listed in Table 2 together with the entropy and enthalpy for the intrinsic ionization (3), denoted m = i in Equation (6) and obtained from the equality $K_i^4 = K_{ox} \cdot K_{red}$ as $\Delta S_i = (\Delta S_{ox} + \Delta S_{red})/4$ and $\Delta H_i = (\Delta H_{ox} + \Delta H_{red})/4$. This enthalpy term can also be looked upon as the electronic band gap in $La_{1/3}Ba_{2/3}Fe^{III}O_{8/3}$. When m = ox (oxidation), Equation (6) contains the defect formation entropy and enthalpy of dissolution of 1 mol of oxygen in a huge excess of the $La_{1/3}Ba_{2/3}Fe^{III}O_{8/3}$ solid. Analogously for the oxygen ex-solution when m = red.

The resulting diagram of the defect contents per formula as functions of p_{O2} and T in Fig. 2 is as expected; increasing temperature promotes electronic defects and makes oxidation harder. The Brouwer diagrams [15] in Fig. 3 give an alternative illustration of this result and complement it by the oxygen content x in $La_{1/3}Ba_{2/3}FeO_x$. Both figures establish the positions of the points of integer Fe^{III} valence, $[e'] = [h^{\bullet}]$, in this bivariate system and illustrate the profound changes in the electronic-defect contents upon exchange of oxygen with surroundings. The slope of the electronic-defect lines at the Fe^{III} point is +1/4 and −1/4 as dictated by Equations (1) and (2). Will the *in-situ* electrical conductivity fit this ideal?

3.3. Electrical conductivity and mobility of the carriers

The electrical conductivity σ was measured isothermally, in small steps upon reduction and oxidation to check the effect of oxygen desorption versus absorption. A test fit of the 977 °C isotherm of σ vs p_{O2} on the decimal-logarithm scale plot in Fig. 4 has a sloped line for each of electronic defects e' and $h^{\bullet}$ and a constant component approximating the contribution from the plateau of the $V_O^{\bullet\bullet}$ charge-carrier content in Fig. 2. The slopes for electronic defects are not far from the ideal model (closer to it at lower temperatures). Given the success of these simple linear fits, the electrical conductivity data were fitted as a bivariate function of p_{O2} and T where the charge-carrier contents per formula are calculated with

Table 2
Thermodynamics of defect-formation reactions (1) (2) (3) in $La_{1/3}Ba_{2/3}Fe^{III}O_{8/3}$.

m	ΔS_m/Jmol^{-1}K^{-1}	ΔH_m/kJmol^{-1}
ox	−107(3)	−112(2)
red	189(8)	722(8)
i	20.5(1)	152(5)

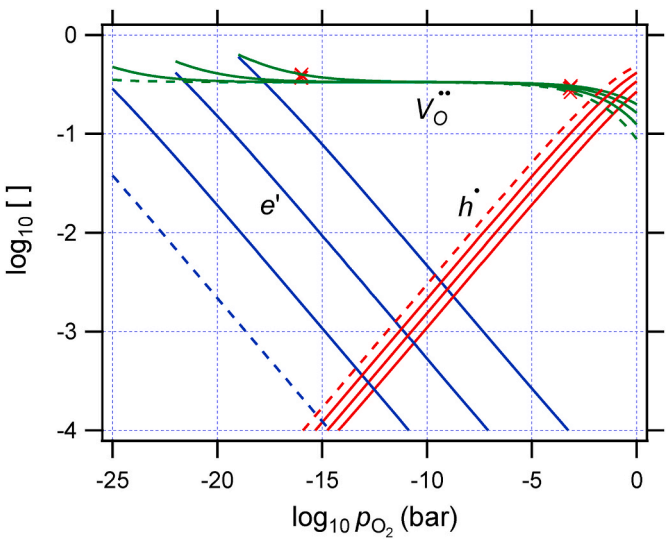

Fig. 2. Contents of electrons, holes and oxygen vacancies per $La_{1/3}Ba_{2/3}FeO_{3-w}$ formula versus partial pressure of oxygen at 977, 838, 727, 636 °C (the latter isotherm dashed) fitted from compositions of quenched samples (crosses) in Table 1.

the defect model of Section 3.2.

The electrical conductivity σ in AV^{-1}m^{-1} of $La_{1/3}Ba_{2/3}FeO_{3-w}$ is a sum of contributions from the considered electronic and ionic charge carriers,

$$\sigma = (e/a^3)\,([e']\mu_{e'} + [h^{\bullet}]\mu_h^{\bullet} + 2[V_O^{\bullet\bullet}]\mu_{VO}^{\bullet\bullet}), \tag{7}$$

where e is the elementary charge in coulombs (C = A•s), and a = 3.9434×10^{-10} m is the unit-cell edge of oxidized $La_{1/3}Ba_{2/3}FeO_{2.9}$ obtained by powder X-ray diffraction of the flat disc when its thickness was measured and the four point contacts attached. The mobility μ_j, in m^{2}V^{-1}s^{-1} = (m/s)/(V/m), of the charge carrier j = e', $h^{\bullet}$, $V_O^{\bullet\bullet}$ was assumed independent of the carrier content per unit cell thus also of p_{O2}. The temperature dependence of defect mobility was expressed with the apparent frequency ν_j (s^{-1}) of the defect j forward progression by unit-cell edge a (m) in linear direction and the apparent activation energy $E_{a,j}$ of that (here taken in eV, hence the factor e that converts eV to J) in Equation (8). With the Boltzmann constant k in J/K, temperature T in K, and J/C = 1 V, the pre-exponential factor in the Arrhenius-type Equation (8) has the dimension of mobility m^{2}V^{-1}s^{-1}:

$$\mu_j = (ea^2\nu_j/kT)\,\exp(-eE_{a,j}/kT) \tag{8}$$

Upon plugging Equation (8) into Equation (7), the a^2 crosses out against a^3. The maximum a = 3.99×10^{-10} m is at $La_{1/3}Ba_{2/3}Fe^{III}O_{8/3}$ [8].

At each point of σ vs p_{O2} and T, the $[V_O^{\bullet\bullet}]$ polynomial (5) with K_m from Equation (6) and parameters from Table 2 is solved for $[V_O^{\bullet\bullet}]$ that converts to $[e']$ and $[h^{\bullet}]$ with K_{ox} and K_{red} of Equations (1) and (2), yielding the three concentrations that enter the combined Equations (8) and (7) for $\sigma = f\{\log(p_{O2}), T\}$. The bivariate fit of this σ via halving the zeroing interval yields the unknown ν_j and $E_{a,j}$ parameters of the three charge-carrier defects j listed in Table 3.

The charge-carrier progression frequencies are close to atomic vibration. As suggested by the activation-energy barriers in Table 3, the hole mobility in Fig. 5 slightly increases with decreasing temperature (the sample also oxidizes), the mobilities of e' and $V_O^{\bullet\bullet}$ (products of reduction) decrease with decreasing temperature.

The conductivity isotherms are plotted in Fig. 6. The fit in the reduced region is good, in the oxidized region it somewhat deviates. The slopes of measured points are slightly higher and curvatures less pronounced than the fit, most so for the highest oxygen content $La_{1/3}Ba_{2/3}FeO_{2.9}$ at p_{O2} = 1 bar and 636 °C (Fig. 3). This is due to the neglected

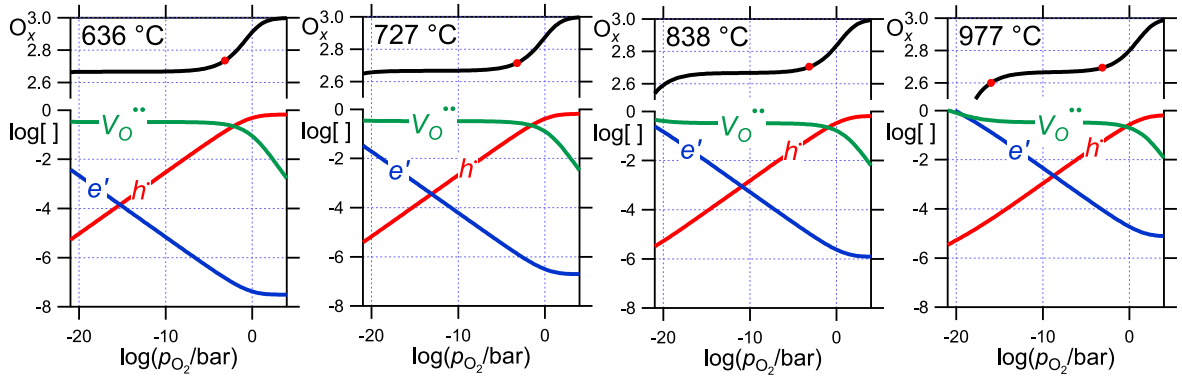

Fig. 3. Brouwer diagrams of main defects in $La_{1/3}Ba_{2/3}FeO_x$ close to the integer valence Fe^{III} of $[e'] = [h^\bullet]$. The neglected $[O_i'']$ that dominates first when $x > 3$ would have plateaued at a low concentration.

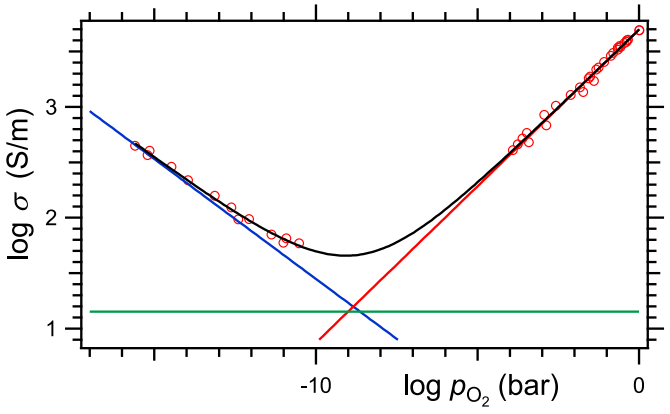

Fig. 4. Sum of ionic and electronic linear components gives the black fitting curve for $La_{1/3}Ba_{2/3}FeO_{3-w}$ electrical conductivity σ vs p_{O2} at 977 °C upon small reductive and oxidative steps. The blue e' line slope is −0.22(2), the red $h^\bullet$ slope 0.282(6). The green line at 14(10) S/m approximates the ionic contribution from the $[V_O^{\bullet\bullet}]$ plateau in Fig. 2.

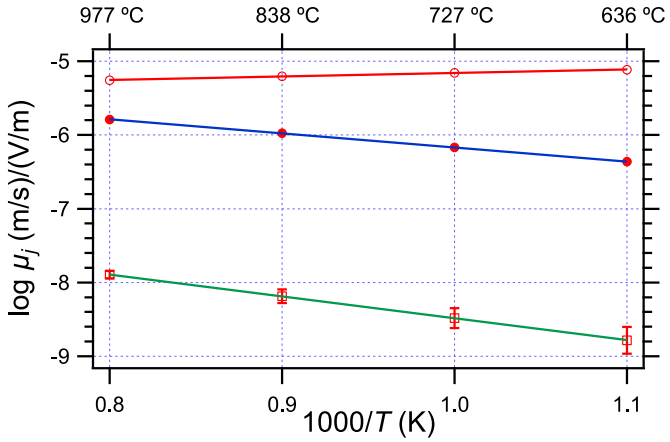

Fig. 5. Mobility of electronic and ionic defects as charge carriers: holes ○, electrons ●, $V_O^{\bullet\bullet}$ □. Standard deviations larger than point symbols are marked.

Table 3
Effective frequency ν and activation energy E_a of the charge-carrier progression by unit-cell edge length in $La_{1/3}Ba_{2/3}FeO_{3-w}$.

j	ν_j/s^{-1}	$E_{a,j}$/eV
$h^\bullet$	3.7(6)×10^{12}	−0.003(16)
e'	8.8(36)×10^{13}	+0.47(4)
$V_O^{\bullet\bullet}$	4.9(49)×10^{12}	+0.68(9)

oxygen interstitials O_i'' of the Frenkel-defect [16] disorder in the ABO_3 prototype, which would prevail first above that composition. Their content would not obtain from the small set of *ex-situ* samples close to the stoichiometric point $La_{1/3}Ba_{2/3}Fe^{III}O_{8/3}$.

Fig. 7 gives the fractional contributions of the individual charge carriers j to the total conductivity; the so called transference numbers t_j plotted versus the equilibrium log(p_{O2}) for the four temperatures. The ionic contribution to the total conductivity increases with decreasing temperature and is significant at oxygen partial pressures below the green bell curves in Fig. 7. Comparison with Fig. 2 shows that the bell-curve tops of ionic conductivity at the minimum electronic conductivity have moved towards lower p_{O2} values. This is because holes in this phase have higher mobility than electrons (Fig. 5), and the hole conductivity then equals electron conductivity first at a more reducing atmosphere that yields a bit more electrons than holes.

After the transference numbers in Fig. 7, the summary overview of the ionic and electronic conductivity contributions follows in Fig. 8. The

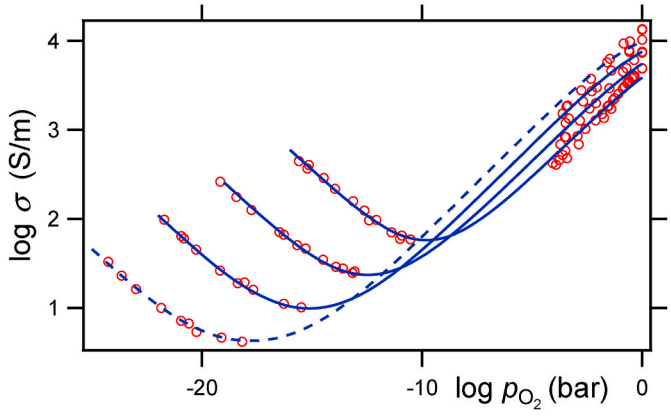

Fig. 6. $La_{1/3}Ba_{2/3}FeO_{3-w}$ electrical conductivity isotherms fitted as functions of p_{O2} for temperatures 977, 838, 727, 636 °C (the latter dashed).

fits confirm that the p_{O2}-independent contribution tested in Fig. 4 is due to oxygen-ionic conductivity that was approximated proportional to the content of oxygen vacancies; neglecting interstitials.

3.4. The kinetics of the oxygen exchange

The gas–solid oxygen-exchange rate can be evaluated from transient curves towards the above-presented electrical conductivities, initiated by the abrupt change of mixing ratio in the gas mixer. At the sample, the

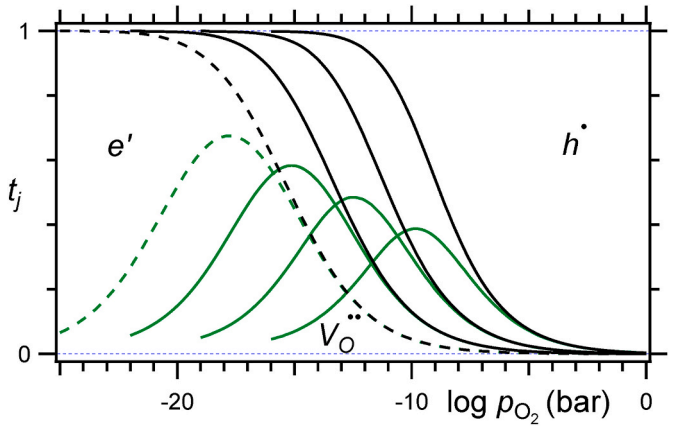

Fig. 7. Transference numbers t_j (conductivity fraction due to charge carrier j) in $La_{1/3}Ba_{2/3}FeO_{3-w}$ vs p_{O2} at 977, 838, 727, 636 °C (the latter dashed). The two plotted isotherms divide the unity into 3 segments; bottom to green isotherm is t_j for $V_O^{••}$, the green to black isotherm is t_j for e', and the black isotherm to top is t_j for $h^•$.

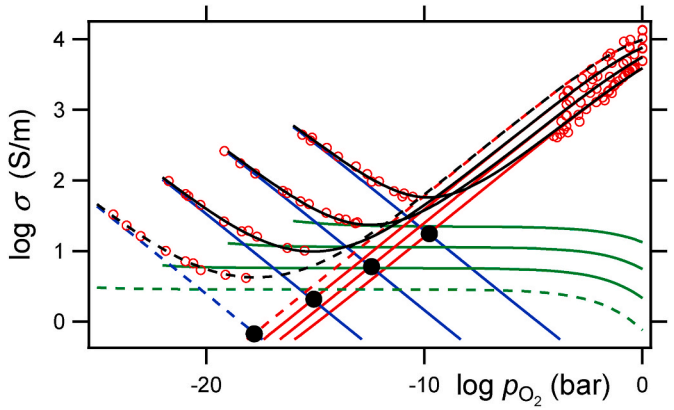

Fig. 8. Ionic (green, $V_O^{••}$) and electronic (blue e', red $h^•$) conductivities that sum to isotherm totals (black) fitted vs p_{O2} at 977, 838, 727, 636 °C (the latter dashed). Black points: $\sigma(e') = \sigma(h^•)$.

gas-composition change is slower and delayed by the flow distance and random motion of the gas. The gradual p_{O2} change around the sample overlaps with the start of the conductivity transient facilitated by oxygen diffusion in the solid to reach the new equilibrium. The measured transients are therefore treated as a diffusion in the solid combined with exponential change of p_{O2} at the sample surface. The conductivity changes were recorded by the Van der Pauw method on isothermal oxygen-absorption and -desorption steps of log(p_{O2}) changed by ~0.5. The transients to the new constant conductivity lasted from about 1 h to 20 h and were recorded in about 50 measurement points.

3.5. Description of the transients

Model of diffusion into half space from both sides of a plane sheet of thickness 2ℓ is used here to describe the flat-disc response upon each transient induced by a small isothermal change in the oxygen partial pressure after the preceding equilibrium. The second Fick law taken in one dimension simplifies upon considering the diffusion coefficient D independent of the minor change in concentration c of oxygen vacancies (content per formula) induced by the transient:

$$\frac{\partial c}{\partial \tau} = D\frac{\partial^2 c}{\partial^2 x} \tag{9}$$

The τ is time, and x is distance. The diffusion is treated as symmetrical about the central plane of the sample disc, where $x = 0$ (the surfaces are at $x = \pm\ell$). Upon the preceding equilibration, the whole range $-\ell < x < +\ell$ obtained the oxygen-vacancy content $c(x,\tau)$ now taken as $c(x,0) = c_0$ of this current equilibration. The gas-mixing ratio is changed, and, after a short period of the gas flow to the hot zone, the p_{O2}-change around the sample starts and initiates at $\tau = 0$ the first σ_{start} differing from the previous equilibrium. At the end of this p_{O2}-change in the gas around the sample, the true equilibrium content c_1 obtains only at the surface, and varies towards the center. The end state of constant conductivity at equilibrium is c_1 throughout the sample. The average concentration in the sheet at the time τ is:

$$\overline{c_\tau} = \frac{1}{2\ell}\int_{-\ell}^{+\ell} c(x,\tau)\mathrm{d}x \tag{10}$$

The extent of the transient response η (0 to 1, like the extent of reaction in chemical kinetics) equals the ratio of the amount M_τ of oxygen released or absorbed at the time τ and its final equilibrium value M_{end}. It is related to the contents c:

$$\eta = \frac{M_\tau}{M_{end}} = \frac{\overline{c_\tau} - c_0}{c_1 - c_0} \tag{11}$$

During the p_{O2}-change in the gas around the sample, it is assumed that the oxygen vacancy content c_{sf} at the sample surface $x = \ell$ approaches the equilibrium concentration c_1 exponentially as a function of time;

$$c_{sf} = c_1\{1 - \exp(-\beta\tau)\} \tag{12}$$

where β is the rate constant (s^{-1}) of the p_{O2}-change in the gas at the sample surface. Because this exponential change correlates with any other surface process, such as the $O_2 \leftrightarrow 2O$ reaction, the whole transient is solved as a combination of the exponential p_{O2}-change and the bulk oxygen diffusion. The $c = c(x,\tau)$ solution of Equation (9) (10) (11) (12) is provided by Crank [17] on page 53:

$$\eta = 1 - \exp(-\beta\tau)\left(\frac{D}{\beta\ell^2}\right)^{\frac{1}{2}}\tan\left(\frac{\beta\ell^2}{D}\right)^{\frac{1}{2}} - \frac{8}{\pi^2}\sum_{n=0}^{\infty}\frac{\exp\left\{-\frac{(2n+1)^2\pi^2}{4\ell^2}D\tau\right\}}{(2n+1)^2\left[1-(2n+1)^2\left\{\frac{\pi^2}{4\beta\ell^2}D\right\}\right]} \tag{13}$$

Equation (13) with n taken up to 100 is fitted by least squares against the array of points from σ_{start} to σ_{end} as $\sigma_0 + \eta(\sigma_{end} - \sigma_{start})$, yielding the oxygen diffusion coefficient D and the rate constant β of the p_{O2}-change around the sample. A 977 °C example plot in Fig. 9 gives the fitted log(D) and log(β) versus the log(p_{O2}) at equilibrium. The β magnitudes suggest

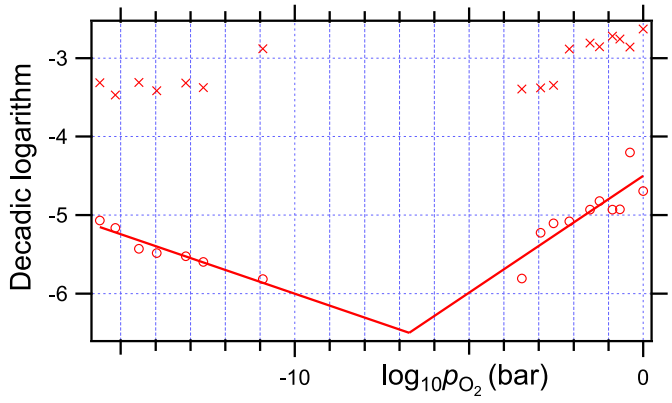

Fig. 9. $La_{1/3}Ba_{2/3}FeO_{3-w}$ oxygen diffusion coefficients as log(D), (○) in cm^2/s for convenient plot, obtained from conductivity transients at 977 °C to the plotted log(p_{O2}). The six leftmost points upon deoxidation, the 7th upon oxidation of the most reduced one. The p_{O2}-change rate parameter β in s^{-1} is given as log(β) marked by crosses ×.

the p_{O2}-change durations from 1 h to 5 h.

The oxygen diffusion coefficient under concentration gradient is smaller than that of the charge carried by oxygen vacancies under electric field. The latter obtains by multiplying the frequency of progression per certain distance (Table 3) by square of that distance, $5(5)\times10^{12}$ s$^{-1}\times(4\times10^{-8})^2$ cm^2, as $8(8)\times10^{-3}$ cm^2/s to be compared with the $\sim10^{-5}$ cm^2/s in Fig. 9. This 10^{-5} cm^2/s value is interpreted with a hopping model of the O atom in Fig. 1 lattice of $N_n = 8$ nearest O neighbors at the progression length $a/2$ in the direction normal to the square of them. The ambipolar-diffusion $D = 10^{-5}$ cm^2/s of Fig. 9 with $a/2 = 1.98\times10^{-8}$ cm yield 2.55×10^{10} forward jumps per second for the hopping-progression rate of the diffusing O atom. What does it say about the probability of the atom hopping in that direction if we consider the atomic vibration frequency $\nu_{at} = 10^{13}$ s^{-1}? It consists of several factors: The probability p_B that one vibration actually overcomes the activation energy so that the O atom jumps to the nearest oxygen site. The probability $p_{avail} = 8[V_O^{\bullet\bullet}]$ that one of the $N_n = 8$ nearest O sites is empty. The probability $p_{dir} = ½$ that the hop is in the given direction. The chance that half of 7 other atoms do not jump into the vacancy left by the O atom before it jumps again is 2/7, hence the probability that this O cannot jump back, the so called correlation factor, is $f_c = 1-(2/7)$ as an estimate. The O-atom progression rate of 2.55×10^{10} s^{-1} then equals:

$$\frac{D}{(a/2)^2} = f_c p_{dir} N_n \left[V_O^{\bullet\bullet}\right] p_B \nu_{at} \quad (14)$$

With $[V_O^{\bullet\bullet}] = ⅑$, Equation (14) yields the Boltzmann probability $p_B = \exp(-\Delta^{\ddagger}G_m/kT) = 8\times10^{-3}$, hence every 125th atomic vibration progresses the O atom in the given direction and $V_O^{\bullet\bullet}$ in the opposite one. Per mole, the Gibbs energy barrier for migration $^{\ddagger}G_m = 50$ kJ/mol at $T = 1250$ K.

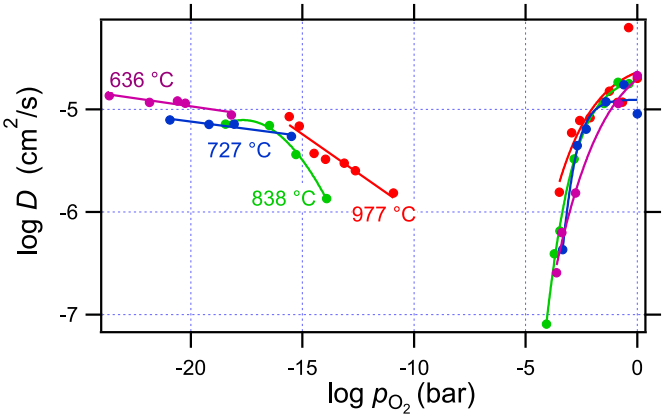

Fig. 10. Oxygen diffusion coefficients D in $La_{1/3}Ba_{2/3}FeO_{3-w}$ from conductivity transients towards end p_{O2} at 636, 727, 838, 977 °C.

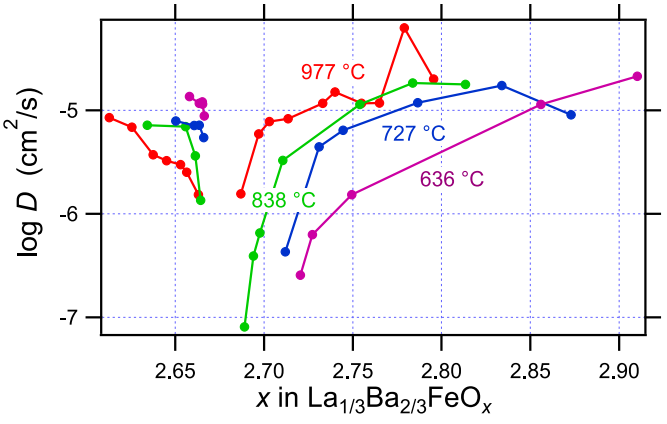

Fig. 11. Oxygen diffusion coefficients D from conductivity transients, replotted against oxygen content x in $La_{1/3}Ba_{2/3}FeO_x$ corresponding to equilibrium (p_{O2}, T) conditions in Fig. 3. Lines connecting the points visualize measurement deviations.

Fig. 10 summarizes the coefficients of oxygen diffusion under concentration gradient as derived from the p_{O2}-change induced transients of alternate-current conductivities at four temperatures. The diffusion coefficients are replotted in Fig. 11 versus the $La_{1/3}Ba_{2/3}FeO_x$ oxygen content x that corresponds via Fig. 3 to the end equilibrium situation of the given diffusion transient. The variation confirms ambipolar character of the oxygen diffusion facilitated by both ionic and electronic defects, where the latter have minimum concentration (Fig. 2) at the Fe^{III} composition $La_{1/3}Ba_{2/3}FeO_{2.667}$. That point in Fig. 11 is in the minimum gap of diffusion coefficients D. The increasing ionic contribution towards lower temperatures (Fig. 7) might be behind the increased D at lower temperatures in the reduced range in Fig. 11.

4. Conclusions

Nine equilibrated and quenched $La_{1/3}Ba_{2/3}FeO_{3-w}$ *ex-situ* samples forming a narrow nonstoichiometry fan around the Fe^{III} point of $w = 1/3$ ($0.26 < w < 0.30$ and $0.36 < w < 0.40$) support defect model of Ba-acceptor doped $LaFeO_3$ simplified by excluding oxygen interstitials that would prevail first above oxygen saturation to ABO_3 perovskite. The defect contents per cubic unit cell are obtained via a bivariate (T, p_{O2}) fit. The electrical conductivity, recorded *in-situ* isothermally upon stepwise equilibrations across a wider nonstoichiometry range from $w \approx 0.39$ under $10^{-15.6}$ bar O_2 at 977 °C to $w \approx 0.09$ under 1 bar O_2 at 636 °C (the w comes from Brouwer diagrams, Fig. 3), is then somewhat underestimated at the oxidized end where oxygen interstitials contribute. Elsewhere along the non-stoichiometry range, the simplified defect model yields a good bivariate (T, p_{O2}) fit of conductivities as a sum of their electronic and ionic components versus p_{O2} at equilibrium. Because the Fe^{III} point stabilizes the compositional plateau where all three oxygens per formula are ⅑ vacant, this perovskite has a relatively high oxygen-ionic conductivity. Evaluation of the conductivity transients upon each stepwise change of p_{O2} into oxygen diffusion coefficients suggests that off the stoichiometric point $La_{1/3}Ba_{2/3}Fe^{III}O_{2.67}$ this oxide becomes a good oxygen-ionic conductor. It could be a good material for oxygen permeation.

Funding

This research did not receive any specific grant from funding agencies in the public, commercial, or not-for-profit sectors.

Declaration of competing interest

The authors declare that they have no known competing financial interests or personal relationships that could have appeared to influence the work reported in this paper.

Data availability

Data will be made available on request.

References

[1] Q. Huang, P. Karen, V.L. Karen, A. Kjekshus, J.W. Lynn, A.D. Mighell, N. Rosov, A. Santoro, Neutron-powder-diffraction study of the nuclear and magnetic structures of $YBa_2Fe_3O_8$ at room temperature, Phys. Rev. B 45 (1992) 9611–9619, https://doi.org/10.1103/PhysRevB.45.9611.

[2] E. García-González, M. Parras, J.M. González-Calbet, M. Vallet-Regí, A new "123" family: $LnBa_2Fe_3O_z$: I. Ln = Dy, Ho, J. Solid State Chem. 104 (1993) 232–238, https://doi.org/10.1006/jssc.1993.1158.

[3] J. Lindén, A. Kjekshus, P. Karen, J. Miettinen, M. Karppinen, A ^{57}Fe Mössbauer study of $REBa_2Fe_3O_{8+w}$ triple perovskites with varied oxygen content (RE = Dy, Er

and Y), J. Solid State Chem. 139 (1998) 168–175, https://doi.org/10.1006/jssc.1998.7828.
[4] J.M. González-Calbet, M. Parras, M. Vallet-Regí, J.C. Grenier, Anionic vacancy distribution in reduced barium-lanthanum ferrites: $Ba_xLa_{1-x}FeO_{3-x/2}$ ($½ \leq x \leq {}^2/_3$), J. Solid State Chem. 92 (1991) 110–115, https://doi.org/10.1016/0022-4596(91)90247-F.
[5] J. Lindén, P. Karen, A. Kjekshus, J. Miettinen, M. Karppinen, Partial oxygen ordering in cubic perovskite $REBa_2Fe_3O_{8+w}$ (RE = Gd, Eu, Sm, Nd), J. Solid State Chem. 144 (1999) 398–404, https://doi.org/10.1006/jssc.1999.8178.
[6] E. García-González, M. Parras, J.M. González-Calbet, M. Vallet-Regí, A new "123" family: $LnBa_2Fe_3O_z$, (II), ln = Nd, Sm, and Eu, J. Solid State Chem. 105 (1993) 363–370, https://doi.org/10.1006/jssc.1993.1226.
[7] J. Lindén, M. Lippmaa, P. Karen, A. Kjekshus, M. Karppinen, A ^{57}Fe Mössbauer study of the cubic perovskite-type phase $LaBa_2Fe_3O_{8+w}$ ($-0.20 < w < 0.83$), J. Solid State Chem. 138 (1998) 87–97, https://doi.org/10.1006/jssc.1998.7757.
[8] P. Karen, A. Kjekshus, Q. Huang, J.W. Lynn, N. Rosov, I. Natali Sora, V.L. Karen, A. D. Mighell, A. Santoro, Neutron and X-ray powder diffraction study of $RBa_2Fe_3O_{8+w}$ phases, J. Solid State Chem. 136 (1998) 21–23, https://doi.org/10.1006/jssc.1997.7636.
[9] P. Karen, A. Kjekshus, Citrate-gel syntheses in the Y(O)–Ba(O)–Cu(O) system, J. Am. Ceram. Soc. 77 (1994) 547–552, https://doi.org/10.1111/j.1151-2916.1994.tb07028.x.
[10] P. Karen, Crystal structure and oxygen nonstoichiometry of $ErBa_2Fe_3O_8$, J. Solid State Chem. 322 (2023), 123953, https://doi.org/10.1016/j.jssc.2023.123953.
[11] P. Karen, Synthesis and equilibrium oxygen nonstoichiometry of $PrBaFe_2O_{5+w}$, J. Solid State Chem. 299 (2021), 122147, https://doi.org/10.1016/j.jssc.2021.122147.
[12] P. Karen, Nonstoichiometry in oxides and its control, J. Solid State Chem. 179 (2006) 3168–3184, https://doi.org/10.1016/j.jssc.2006.06.012.
[13] L.J. van der Pauw, A method of measuring the resistivity and Hall coefficient on lamellae of arbitrary shape, Philips Tech. Rev. 20 (1958/59) 220–224.
[14] F.A. Kröger, Defect chemistry in crystalline solids, Annu. Rev. Mater. Sci. 7 (1977) 449–475, https://doi.org/10.1146/annurev.ms.07.080177.002313 (and references therein).
[15] G. Brouwer, A general asymptotic solution of reaction equations common in solid-state chemistry, Philips Res. Rep. 9 (1954) 366–376.
[16] J. Frenkel, Über die Wärmebewegung in festen und flüssigen Körpern, Z. Phys. 35 (1926) 652–669, https://doi.org/10.1007/BF01379812.
[17] J. Crank, The Mathematics of Diffusion, second ed., Oxford University Press, 1975.